

# Sb-Mediated Tuning of Growth- and Exciton Dynamics in Entirely Catalyst-Free GaAsSb Nanowires

Hyowon W. Jeong,\* Akhil Ajay, Haiting Yu, Markus Döblinger, Nitin Mukhundhan, Jonathan J. Finley, and Gregor Koblmüller\*

Vapor-liquid-solid (VLS) growth is the mainstream method in realizing advanced semiconductor nanowires (NWs), as widely applied to many III-V compounds. It is exclusively explored also for antimony (Sb) compounds, such as the relevant GaAsSb-based NW materials, although morphological inhomogeneities, phase segregation, and limitations in the supersaturation due to Sb strongly inhibit their growth dynamics. Fundamental advances are now reported here via entirely catalyst-free GaAsSb NWs, where particularly the Sb-mediated effects on the NW growth dynamics and physical properties are investigated in this novel growth regime. Remarkably, depending on GaAsSb composition and nature of the growth surface, both surfactant and anti-surfactant action is found, as seen by transitions between growth acceleration and deceleration characteristics. For threshold Sb-contents up to 3–4%, adatom diffusion lengths are increased  $\approx$ sevenfold compared to Sb-free GaAs NWs, evidencing the significant surfactant effect. Furthermore, microstructural analysis reveals unique Sb-mediated transitions in compositional structure, as well as substantial reduction in twin defect density,  $\approx$ tenfold over only small compositional range (1.5–6% Sb), exhibiting much larger dynamics as found in VLS-type GaAsSb NWs. The effect of such extended twin-free domains is corroborated by  $\approx$ threefold increases in exciton lifetime ( $\approx$ 4.5 ns) due to enlarged electron-hole pair separation in these phase-pure NWs.

and inherent 1D structure that enables effective monolithic integration onto lattice mismatched substrates—such as silicon (Si)—with very small footprint. This has led to extensive research activities and developments of diverse III-V NW-based electronic, optoelectronic, and photonic device applications, including vertical gate-all-around transistors,<sup>[1,2]</sup> efficient NW solar cells,<sup>[3–6]</sup> NW lasers<sup>[7–10]</sup> and light-emitting diodes,<sup>[11,12]</sup> as well as quantum light sources.<sup>[13–15]</sup>

Amongst the different III-V NW materials, the antimony (Sb) based ternaries, in particular GaAsSb NWs, are classified as important materials due to numerous interesting properties: GaAsSb offers wide tunable band gap over the near infrared and telecom spectral range ( $\approx$ 0.8–1.5  $\mu$ m), high carrier mobility, and high optical absorption coefficient. Especially, the low hole effective mass of GaAsSb enables remarkably high hole mobility, which is attractive for high-speed optoelectronic applications, such as high-speed photodetectors<sup>[16–18]</sup> and laser diodes.<sup>[19]</sup> The conductivity of intrinsic GaAsSb can be; however, also controlled from p-type (Sb-rich GaAsSb) towards n-type (As-rich GaAsSb) by tailoring alloy composition. Simple adjustment of compositional parameters enables also engineering of band alignments of both type-I to type-II in purely GaAsSb-based heterojunctions.<sup>[20]</sup> All this provides very unique scope for advanced device engineering using just a single material system, as has been exemplified in various GaAsSb-NW devices.<sup>[21,22]</sup>


To date, extensive work was performed on tuning the composition and resulting structural and electronic properties of GaAsSb-based NWs, using the conventional vapor-liquid-solid (VLS) growth method. In VLS growth, the presence of Sb was found to inhibit axial NW growth, while promoting radial growth with increasing Sb supply,<sup>[23–26]</sup> irrespective of the employed droplet catalyst (Au- or self-catalyst). This behavior was attributed to arise from the so-called Sb poisoning effect, which blocks Ga diffusion and results in consecutive reduction of group-V supersaturation in the droplet catalyst.<sup>[25]</sup> The incorporation of Sb has also remarkable effects on the crystal structure, leading to predominantly zinc-blende (ZB) crystal phase (with occasional twin-plane defects) in GaAsSb NWs, even under conditions where Sb-free GaAs NWs crystallize under

## 1. Introduction

Free-standing III-V semiconductor nanowires (NW) are very attractive materials due to their unique physical properties

H. W. Jeong, A. Ajay, H. Yu, N. Mukhundhan, J. J. Finley, G. Koblmüller  
Walter Schottky Institute  
TUM School of Natural Sciences  
Technical University of Munich  
85748 Garching bei München, Germany  
E-mail: hyowon.jeong@wsi.tum.de; gregor.koblmue@wsi.tum.de

M. Döblinger  
Department of Chemistry  
Ludwig-Maximilians-Universität München  
81377 Munich, Germany

 The ORCID identification number(s) for the author(s) of this article can be found under <https://doi.org/10.1002/smll.202207531>.

© 2023 The Authors. Small published by Wiley-VCH GmbH. This is an open access article under the terms of the Creative Commons Attribution-NonCommercial-NoDerivs License, which permits use and distribution in any medium, provided the original work is properly cited, the use is non-commercial and no modifications or adaptations are made.

DOI: 10.1002/smll.202207531

the wurtzite (WZ) phase.<sup>[27]</sup> Recent work also reckoned that twin-free ZB segments with extended lengths could be realized when increasing the Sb supply.<sup>[23,27]</sup>

Quite interestingly, entirely catalyst-free, vapor-solid (VS) growth of GaAsSb NWs—free of any droplet catalyst—was hardly explored so far. Only most recently, Ajay et al. developed selective area epitaxy (SAE) of GaAs(Sb) NWs on patterned Si(111) substrates, showing that the addition of small trace amount of Sb (1–2%) leads to surprising enhancements in the axial NW growth.<sup>[28]</sup> This contrasts the typical growth-limiting effect of Sb observed in VLS growth studies.<sup>[23–26]</sup> Despite these intriguing observations, no clear understanding of the obvious Sb self-surfactant effect on the growth dynamics could yet be obtained in catalyst-free GaAsSb NWs; for example, it remains fully unclear how the Sb self-surfactant effect scales with Sb-supply (content), for example, if there is a threshold Sb-content required and whether the surfactant effect persists toward higher Sb-content. Moreover, there is no specific knowledge of the surface diffusion lengths of adatoms under the presence of Sb, and how increased Sb-content affects the structural and optical properties in such non-catalytic GaAsSb NWs, suggesting that more comprehensive studies are needed.

Against this background, we systematically explore the Sb-mediated morphological, microstructural, and optical properties of catalyst-free, VS-type GaAsSb NWs grown by selective area molecular beam epitaxy (MBE). By correlating NW morphology and composition we clearly delineate regimes where Sb behaves as surfactant, enhancing adatom diffusion and axial growth, as well as regimes of anti-surfactant action. Furthermore, by tracing the NW lengths with respect to growth

time and identifying growth rate scaling characteristics, we are able to determine very high adatom diffusion lengths on the NW sidewalls of GaAsSb NWs compared to Sb-free GaAs NWs. Ultimately, structure-property relationships are identified by mapping the Sb-dependent evolution of microstructure, for example, lengths of defect-free ZB domains, in individual GaAsSb NWs and correlate them with the resulting exciton dynamics. Thereby, we obtain important insights into the Sb surfactant mediated influences on the structural- and optical properties of non-catalytic GaAsSb NWs. All NW samples are grown on SiO<sub>2</sub>-masked Si(111) substrates with lithographically defined mask openings (at given pitch), and subsequent characterization of morphology, structure, and optical properties is carried out by various electron microscopy and state-of-the-art micro-photoluminescence methods. All details about growth and characterization are seen in the Experimental Section.

## 2. Results and Discussion

### 2.1. Sb- and Geometry Parameter-Dependent Morphological Properties

To show the Sb-dependent morphology evolution of the as-grown GaAsSb NW arrays, exemplary scanning electron microscopy (SEM) images are shown in **Figure 1a,b** at 500 nm pitch and two SiO<sub>2</sub> mask opening sizes ( $d_0$ ) of 20 nm and 70 nm, respectively. The growth time for these samples was 90 min, and growth temperature was 630°C. It is clearly seen that without Sb (GaAs NWs) only few and extremely short NWs were

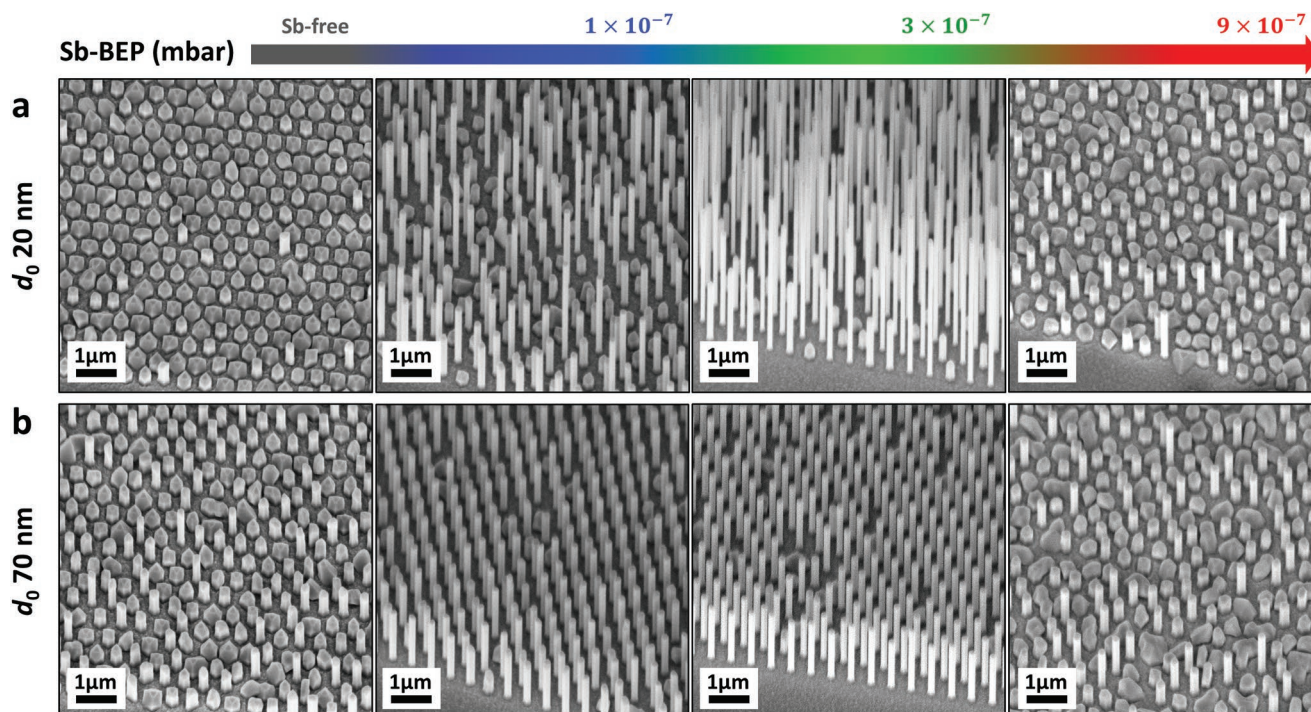


**Figure 1.** SEM images of selective area epitaxial (SAE)-grown GaAsSb NW arrays with pitch 500 nm and SiO<sub>2</sub> mask opening diameter ( $d_0$ ) of (a) 20 nm and (b) 70 nm, grown for 90 min under varying Sb-BEP from 0 (Sb-free GaAs, left) to  $9 \times 10^{-7}$  mbar (right), respectively. Images were taken at 45° and tilt corrected to display real lengths.

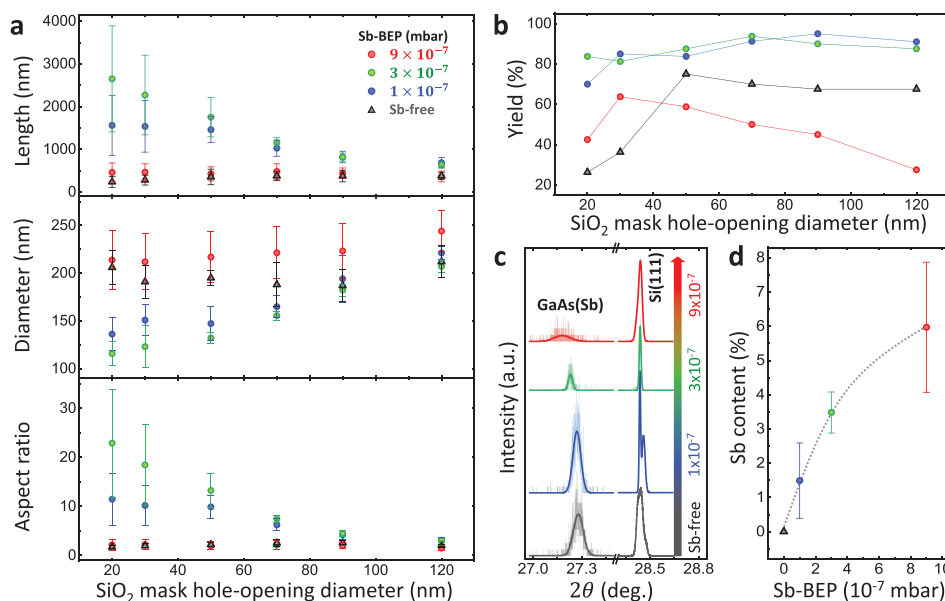


**Figure 2.** Quantitative evolution of a) the average NW length, diameter, and aspect ratio and b) growth yield with respect to nominal SiO<sub>2</sub> mask opening diameter at 500 nm pitch. c) Spectra with fit functions from HRXRD  $2\theta - \omega$  scans on the as-grown NW arrays (Si (111) diffraction peaks are factorized) and d) the extracted Sb-molar fraction in the GaAsSb NWs as a function of Sb-BEP.

produced, while extended crystallites appear as the major structures within the arrays. In contrast, addition of small amount of Sb flux, Sb-BEP (beam equivalent pressure) of  $1 \times 10^{-7}$  mbar, strikingly improves the NW growth yield and lengths compared to Sb-free GaAs NWs, which are even further enhanced by increasing Sb-flux to intermediate Sb-BEP of  $3 \times 10^{-7}$  mbar. However, for higher Sb-BEP of  $9 \times 10^{-7}$  mbar, the growth yield and NW lengths significantly drop, resulting also in many short crystallites and clusters, similar to the Sb-free GaAs NWs.

To quantitatively describe the morphological evolution of each NW sample,  $d_0$  dependent NW lengths ( $L$ ), diameters ( $D = 2R$ ) and aspect ratios ( $A.R. = L/D$ ) are plotted in **Figure 2a** for different Sb-BEPs, and compared with Sb-free GaAs NWs. For each sample, NW growth yields are also shown in **Figure 2b**. Note that extremely short crystallites and clusters were not considered in this analysis. In all GaAsSb NW samples, an inverse trend of NW length and diameter is observed which is characteristic of the non-catalytic growth mode<sup>[28–31]</sup>; specifically, with decreasing  $d_0$  from 120 nm to 20 nm, the GaAsSb NWs show increasing length and decreasing diameter, yielding enhanced aspect ratio. These trends are most pronounced in NW-arrays with low to intermediate Sb-BEP, and only vaguely seen in the arrays with highest Sb-BEP due to the inhibited axial growth. The Sb-free GaAs NWs evidence, however, a somewhat different trend; first the expected rise in NW length (decrease in diameter) when tuning  $d_0$  from 120 nm towards smaller openings, but this trend suddenly reverses for mask opening sizes smaller than  $\approx 80$  nm. This observation resembles previous findings in pure GaAs NWs, as was reported elsewhere.<sup>[32]</sup>

To obtain direct correlation between the very different NW growth behavior and the actual alloy composition, we performed high-resolution X-ray diffraction (HRXRD)  $2\theta - \omega$  scans on the samples of standing NW arrays grown with

different Sb-fluxes. The respective HRXRD data with GaAsSb peak reflections are shown in **Figure 2c**, along with the corresponding Sb molar fraction plotted as a function of the applied Sb-flux in **Figure 2d**. As expected, the GaAsSb peak reflections shift to smaller  $2\theta$  angles with increasing Sb-flux, reflecting the increase in the in-plane lattice parameter due to increased Sb incorporation. By employing Vegard's law and assuming that the epitaxial strain is fully relaxed in the NWs, we obtained Sb molar fractions that increase from  $\approx 1.5\%$  to  $\approx 6\%$  for Sb-BEP increasing from  $1 \times 10^{-7}$  mbar to  $9 \times 10^{-7}$  mbar. Interestingly, for low Sb-BEP the Sb-content rises monotonically with Sb-BEP, but this trend discontinues with less efficient Sb incorporation towards higher Sb-BEP (see guide to the eye). This saturation behavior is analogous to planar GaAsSb thin films, and can be understood by the peculiar surface segregation and incorporation dynamics of Sb. It is well known that due to its small surface energy and large atomic radius, Sb tends to float on the growth surface, forming a dissociative Sb surface segregation layer.<sup>[33,34]</sup> In dynamic equilibrium, this Sb-rich surface layer promotes an As exchange reaction in existing Ga-Sb bonds and thereby inhibits incorporation of Sb atoms, especially for high critical Sb surface coverages.<sup>[34,35]</sup> The presence versus absence of such critical Sb segregation layer has intriguing consequences for many aspects in growth, as well as structural and compositional properties as we show below.

Crucially, the growth dynamics such as axial growth rate and aspect ratio, also show discontinuous scaling behavior with alloy composition (Sb-content), and in fact are very different from previous growth studies on NWs. Consistently, all previous reports on Sb-containing III-V NWs noted that the addition of Sb suppresses axial growth in a rather continuous way, irrespective of the employed growth method.<sup>[24,25,36]</sup> In stark contrast, our results show that in the limit of small Sb-molar

fraction the axial growth is substantially increased, confirming the recently suspected Sb self-surfactant effect in non-catalytic GaAsSb NWs.<sup>[28]</sup> For example, as seen in Figure 2a, small Sb-content of 1.5% yields already a  $\approx$ fivefold increase in aspect ratio compared to Sb-free GaAs NWs, while the enhancement in aspect ratio is even  $\approx$ tenfold for further increased Sb-content of 3.5%. This suggests that even minute amounts of Sb affect the growth dynamics substantially, and Sb-content up to  $\approx$ 3–4% yields maximum growth enhancement under the given growth conditions. This allows us to accurately delineate the range of Sb molar fractions for achieving highest possible axial growth, as required for specific NW device applications. However, this trend discontinues for higher Sb-content; NW arrays with Sb-content of 6% result in much lowered aspect ratio that is nearly the same as for Sb-free NWs. It therefore appears that for higher Sb-content the growth dynamics start to approach the common Sb-limiting growth behavior, reported in literature.<sup>[24,25]</sup> This is quite interesting because it suggests that depending on the Sb supply, Sb can act both as a surfactant (enhancing growth, limit of small Sb-content  $\approx$ 1.5–4%) and as an anti-surfactant (limiting growth, high Sb-content > 4–6%). This cross-over in surfactant action seems to be correlated with the transition in Sb-incorporation behavior discussed in the compositional data above in Figure 2d. Based on the widely accepted Sb surface segregation model, we suspect that for very low Sb supply the adatom coverage of Sb residing on the growth surface is so low (sub-critical coverage) that the surface mimics an As-rich surface reconstruction,<sup>[37]</sup> favoring increased adatom diffusion. In contrast, for larger Sb supply a transition to a Sb-rich surface reconstruction with significant Sb surface coverage can be anticipated, based on observations in planar layers.<sup>[34,35,37]</sup> Under such Sb-enriched surface, both As and Ga adatoms rapidly exchange their overlayer site for a sub-surface site, which strongly inhibits their adatom diffusion,<sup>[38]</sup> limiting axial growth. Below, we illustrate the effects of Sb-mediated adatom diffusion behavior in a more comprehensive way.

Although directing our observations, in the following, mainly to the limit of small Sb-content, we wish to point out that—in general—NWs with high axial growth rate (aspect ratio) at further increased Sb-content, much beyond 6%, should be feasible by adjusting growth conditions. Such optimization was recently demonstrated in SAE-growth of mixed III-V-V ternary NWs (e.g., VS-type InAsSb NWs) performed under similar MBE conditions.<sup>[36]</sup> Herein, not only tuning of growth temperature and V/III ratio (growth rate), but also extending interwire separation to large pitch were found to effectively increase both Sb-content and aspect ratio due to reduced competition for Sb adatoms in sparse NW arrays. Similar effects are also observed in the present GaAsSb NWs, where a considerable influence of pitch (Figures S1 and S2, Supporting Information) and growth temperature (Figure S3, Supporting Information) on Sb incorporation and aspect ratio of GaAsSb NWs are found.

## 2.2. Effect of Sb on Nanowire Growth Dynamics

To further illustrate the anticipated Sb self-surfactant behavior in the limit of low Sb-content, we present in the following a description of the surface diffusion enhancements based on a

growth time series performed on GaAsSb NWs. Here, we compare the axial growth dynamics of GaAsSb NW arrays grown at fixed Sb-BEP of  $3 \times 10^{-7}$  mbar (Sb-content of  $\approx$ 3.5%) with Sb-free GaAs NWs, when grown for different growth times ( $t_{\text{growth}}$ ) ranging from 15 min up to 150 min. Figure 3a,b shows exemplary SEM images of GaAsSb NWs ( $t_{\text{growth}} = 15, 90$  and 150 min) and Sb-free GaAs NWs ( $t_{\text{growth}} = 15, 90$  and 120 min), for the same geometrical parameters ( $p = 500$  nm and  $d_0 = 70$  nm), respectively. A first striking observation is that the GaAsSb NWs keep growing axially until  $t_{\text{growth}} = 150$  min (and probably beyond), resulting in surprisingly high aspect ratio, while the axial growth of Sb-free GaAs NWs saturates already well before  $t_{\text{growth}} = 120$  min, highlighting the strong effects of Sb on the axial growth of GaAsSb NWs.

For more quantitative analysis of the growth dynamics, we plot in Figure 3c the evolution of the average axial growth rates ( $R_L = L/t_{\text{growth}}$ , red-line) and radial growth rates ( $R_R = R/t_{\text{growth}}$ , blue-line) of each NW sample as a function of growth time. Overall, both GaAs and GaAsSb NWs exhibit similar trends; during the incipient phase of the growth ( $t_{\text{growth}} \approx 15$  min) it is clearly seen that growth occurs predominantly in the radial direction, leading to low aspect ratios, since the catalyst-free vapor-solid growth mode is initially dominated by surface diffusion of Ga adatoms on the SiO<sub>2</sub>-masked Si (111) substrate.<sup>[39–41]</sup> For longer growth times ( $t_{\text{growth}} = 60$  min and beyond), the radial growth saturates rapidly and the axial growth becomes dominant. This is expected since more adatoms can impinge on the NW sidewall surfaces, thus contributing to surface diffusion and axial growth.<sup>[39–41]</sup> Under such impingement dominated growth, where all surface diffusing species, that is, Ga adatoms, reach the NW tip, one expects a highly non-linear axial growth rate with time,<sup>[41]</sup> since the impingement rate scales with the increasing capture area of the growing sidewall surfaces. Indeed, as shown in Figure 3c, such non-linear enhancement in axial growth rate is observed for longer growth times. Finally, as NWs grow even longer, that is, longer than the surface diffusion length of the Ga adatoms, the axial growth rate starts to saturate, transforming to a sidewall diffusion limited growth regime.<sup>[39–41]</sup>

Most importantly, from the direct comparison of GaAsSb and Sb-free GaAs NW arrays (Figure 3c), we find that the GaAsSb NWs exhibit a highly accelerated, non-linear increase in axial growth rate up to a maximum of  $\approx 30$  nm min<sup>-1</sup> until  $t_{\text{growth}} = 120$  min, beyond which the rate tends to level off, marking the transition to sidewall diffusion-limited growth. Similarly, the axial growth rate of the GaAs reference NWs increases also non-linearly, but only up to a maximum of  $\approx 6$  nm min<sup>-1</sup>, and the transition to diffusion-limited growth sets in much earlier ( $t_{\text{growth}} = 90$  min). Based on these observations we can estimate the diffusion length of Ga adatoms by the cross-over from impingement dominated, non-linear growth to saturated, steady-state growth. We find the Ga adatom diffusion length on the GaAsSb NWs under the given conditions to be  $\approx 3600$  nm, that is, nearly 7 times longer than the estimated diffusion length of only  $\approx 540$  nm in Sb-free GaAs NWs. This strong enhancement in Ga surface diffusion length clearly verifies the anticipated Sb surfactant effect in the limit of small Sb molar fractions.

The strong surface diffusion enhancement in the presence of Sb is also displayed in Figure 3d, by plotting the axial growth

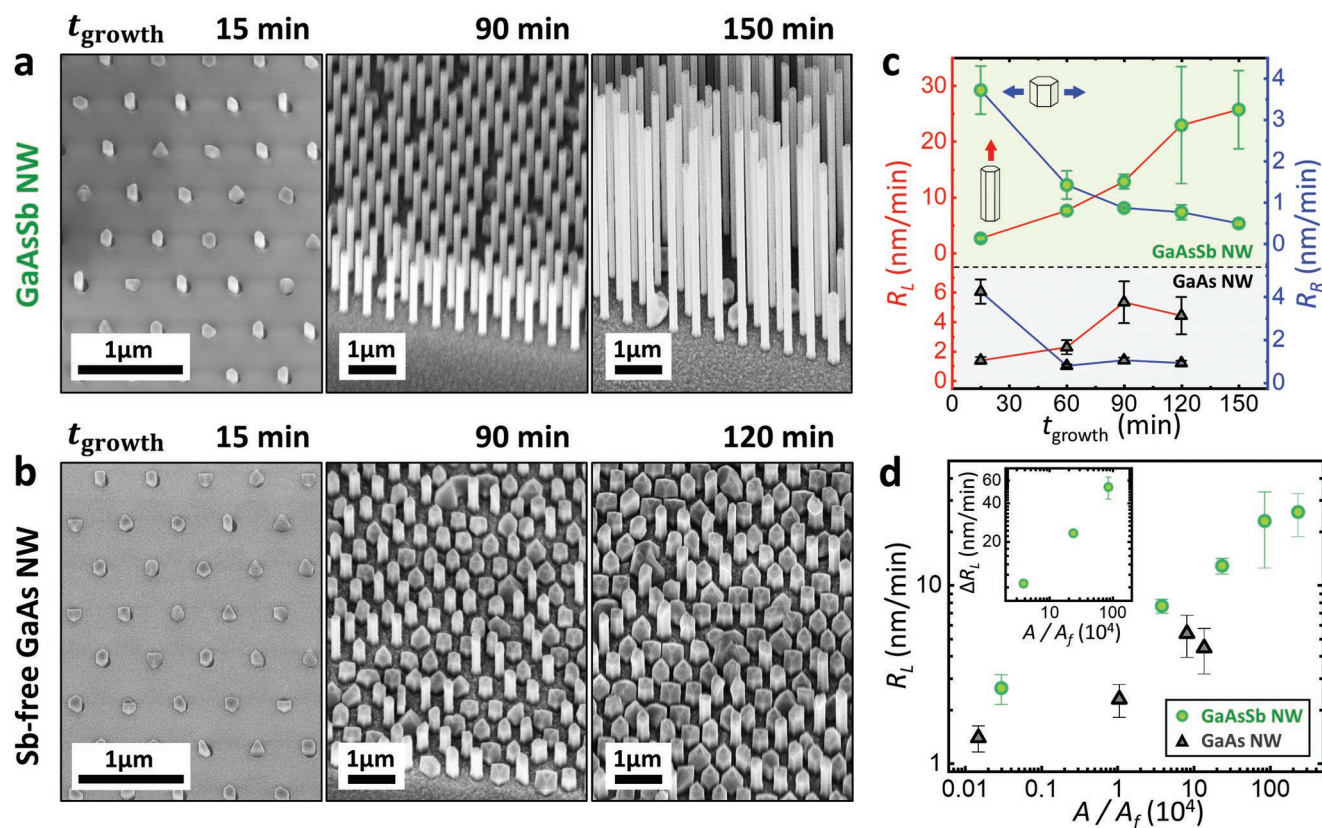


**Figure 3.** a) SEM images of as-grown GaAsSb NW arrays with a fixed Sb-BEP of  $3 \times 10^{-7}$  mbar and b) Sb-free GaAs counterpart with varying growth time ( $t_{\text{growth}}$ ) at  $p = 500$  nm and  $d_0 = 70$  nm. Images were taken at  $45^\circ$  and tilt corrected to display real lengths. c) Evolution of average axial ( $R_L$ , red-line) and radial growth rates ( $R_R$ , blue-line) of GaAsSb NWs (top, green circles) and Sb-free GaAs NWs (bottom, black triangles) as a function of growth time ( $t_{\text{growth}}$ ). d)  $R_L$  evolution of GaAsSb and GaAs NWs with respect to NW sidewall surface area in log-log scale normalized to the top-facet surface area ( $A/A_f$ ). Inset: step axial growth rates of GaAsSb NWs in each growth time interval ( $\Delta R_L$ ) at 60 min, 90 min, and 120 min.

rate as a function of sidewall surface area ( $A$ ) in log-log scale normalized to the top-facet surface area ( $A_f$ ) at the given growth time. In this representation, we can also confirm that growth of GaAsSb NWs is governed for most parts by direct impingement and subsequent diffusion, where the growth rate is expected to scale linearly with increasing sidewall surface area. Indeed, the non-linear evolution of  $R_L$  with respect to  $t_{\text{growth}}$  (Figure 3c) translates very well to a linear relationship of  $R_L$  over  $A/A_f$  (Figure 3d) for extended growth time ( $t_{\text{growth}} = 60\text{--}120$  min), and levels off for longest growth time as the NW exceeds the diffusion length. The inset in Figure 3d shows step axial growth rates of the GaAsSb NWs in each growth time intervals ( $\Delta R_L = \Delta L/\Delta t_{\text{growth}}$ ) between 60 min, 90 min and 120 min, allowing for more precise estimation of the respective growth rates at each growth time step. The linear relationship in log-log plot confirms that in this growth time range the axial growth of GaAsSb NWs is not diffusion-limited at all. Instead, growth is clearly governed by direct impingement and sufficient sidewall diffusion of Ga adatoms to the NW tip due to the enhanced diffusion length. Likewise, similar trends in  $R_L$  versus  $A/A_f$  can also be inferred from the Sb-free GaAs NWs, but transition to diffusion-limited growth occurs at substantially reduced sidewall surface area (growth time). To microscopically explain the strongly enhanced surface diffusion, we can only speculate at the moment about the origins of such peculiar Sb action, by

referring to knowledge based on planar layers. We suggest that the surface energetics must be clearly modified, for example, by alterations in the usual As-rich surface reconstruction via different Sb surface atomic densities, which influence surface diffusion.<sup>[33–35,37,38]</sup> Further experiments, such as desorption mass spectrometry highlighting sub-critical Sb surface coverages, as well as analysis of Sb-mediated surface structure via scanning tunneling microscopy and X-ray photoemission studies, along with atomistic modelling will be necessary for fully complete understanding.

### 2.3. Sb-Mediated Microstructural Properties

To characterize the Sb-dependent microstructural properties of individual NWs, high-resolution (HR) HAADF-STEM (high-angular annular dark field – scanning transmission electron microscopy) was conducted on the three SAE-grown GaAsSb NW samples with varying Sb-BEP. Hereby, NWs were transferred from identical SAE fields ( $p = 500$  nm and  $d_0 = 70$  nm) onto carbon-coated copper grids, to allow for best possible comparison. Representative HAADF-STEM micrographs as recorded from a central section of the NWs are shown in **Figure 4a–c** for GaAsSb NWs grown with Sb-BEP of  $1 \times 10^{-7}$  (1.5% Sb),  $3 \times 10^{-7}$  (3.5% Sb) and  $9 \times 10^{-7}$  mbar (6% Sb).

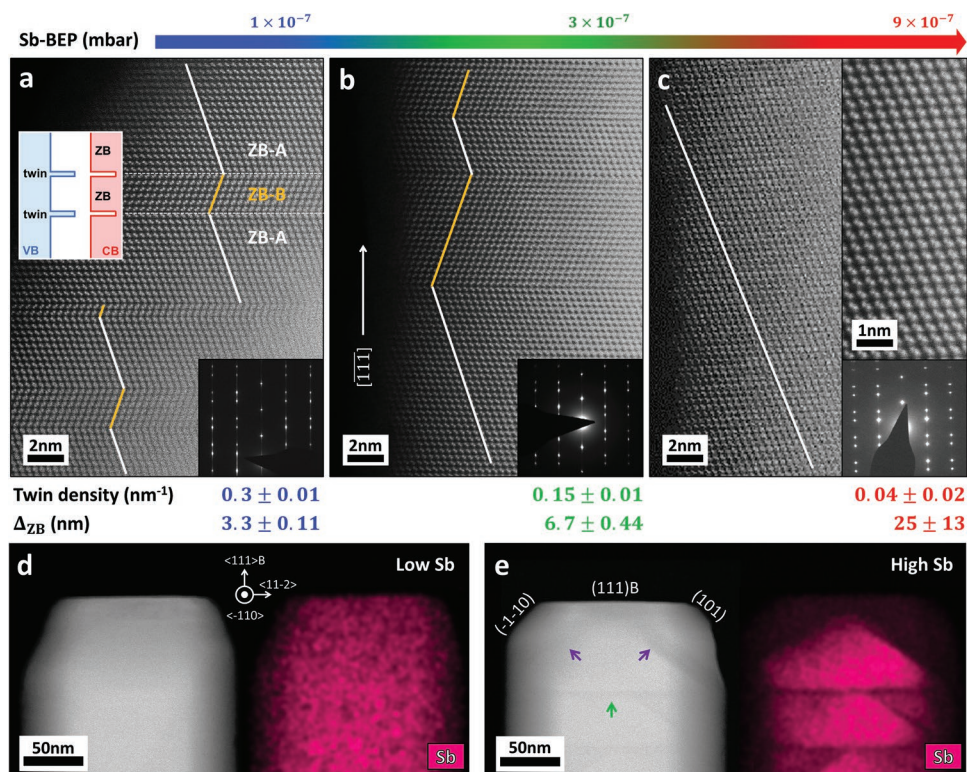


**Figure 4.** HR-HAADF-STEM micrographs of representative GaAsSb NWs with varying Sb-BEP of a)  $1 \times 10^{-7}$  (inset: band diagram of rotational twins of the ZB structure), b)  $3 \times 10^{-7}$ , and c)  $9 \times 10^{-7}$  mbar (inset: high-magnification view of the twin-free domain). Associated SAD patterns are also shown in respective insets. White and orange solid lines indicate alternating rotational twin domains. Estimated twin density and the resulting mean length of the twin-free ZB domain ( $\Delta_{\text{ZB}}$ ) are displayed at the bottom, respectively. Bottom panels show lower resolution HAADF-STEM micrographs and associated EDX maps of the Sb distribution from the top regions of the GaAsSb NWs grown with d) lowest Sb-BEP ( $1 \times 10^{-7}$  mbar) and e) highest Sb-BEP ( $9 \times 10^{-7}$  mbar). Contrast modulations across (111)B and inclined  $\{-110\}$  facets are marked as green and purple arrows, respectively.

As recognized from the micrographs as well as the respective SAD patterns (insets), all samples exhibit pure ZB-phase with rotational twin domains only (ZB-A and ZB-B). This observation agrees well with previous studies of both non-catalytic<sup>[28]</sup> and catalyst-assisted GaAsSb NWs,<sup>[23,25,42]</sup> where the addition of Sb was found to inhibit formation of WZ phase and, hence, eliminates polytype intermixing and related stacking defects with hexagonal stacking component as otherwise seen in Sb-free GaAs NWs.<sup>[29,42,43]</sup> Indeed, it has been understood that the formation of a rotational twin defect in ZB crystals, which originates due to a transition from ZB to WZ structure, can be attributed to the relatively low energy for its formation.<sup>[45]</sup> Such a transition may not be as favorable in Sb-based III-V NWs due to the much smaller ionic bonds (low crystal ionicity) of the III-Sb materials than III-As materials, leading to a higher stability of the ZB (cubic) phase than the WZ (hexagonal) structure.<sup>[46–48]</sup> However, so far, in the much less studied non-catalytic GaAsSb NWs the ZB-domain structure and twin-defect evolution with Sb-content has not been quantified.

To perform such quantitative analysis, we counted the number of twin domains along the entire length of each NW for statistically relevant data and compare the results with the STEM micrographs depicted in Figure 4a–c. Here, we marked individual, alternating twin domains (ZB-A, ZB-B) with white and orange solid lines, and the data clearly shows that with increasing Sb-content twin-free domains become more

extended, leading to significantly reduced twin defect densities. While individual twin domains are still relatively short in GaAsSb NWs with lowest Sb-content (Figure 4a), NWs with higher Sb-content (Sb-BEP =  $9 \times 10^{-7}$  mbar) show much longer twin-free ZB domains—note, in Figure 4c, there is not even a single twin defect observed along the recorded section (see also inset, higher magnification micrograph). In this NW the length of such twin-free ZB domain can even be as long as  $\approx 40$  nm. More quantitatively, the mean lengths of twin-free ZB domains ( $\Delta_{\text{ZB}}$ ), as extracted from each NW sample, is found to increase from  $\Delta_{\text{ZB}} = 3.3 \pm 0.11$  nm (Sb-BEP =  $1 \times 10^{-7}$  mbar), to  $6.7 \pm 0.44$  nm (Sb-BEP =  $3 \times 10^{-7}$  mbar), and up to  $25 \pm 13$  nm (Sb-BEP =  $9 \times 10^{-7}$  mbar) with increasing Sb-flux (see also Figure 6b below). This corresponds to a substantial decrease in twin defect density from  $\approx 0.3 \pm 0.1$  twins  $\text{nm}^{-1}$  (Sb-BEP  $1 \times 10^{-7}$  mbar) to  $0.15 \pm 0.1$  twins  $\text{nm}^{-1}$  (Sb-BEP  $3 \times 10^{-7}$  mbar), and even further down to  $0.04 \pm 0.02$  twins  $\text{nm}^{-1}$  (Sb-BEP of  $9 \times 10^{-7}$  mbar), respectively. Interestingly, we recognize that in the limit of low Sb-content the reduction in twin defect density scales proportionally with Sb-BEP. But, for higher Sb-BEP, the twin defect density drops (resp. twin-free segment length increases) very abruptly, much more than expected from the proportionality (cf. Figure 6b). We attribute this marked change to the cross-over in surface structure, where the Sb-rich surface (dissociative Sb segregation layer, as discussed above) limits the formation of twins much more substantially. This is expected because

such Sb-rich surface crucially lowers the crystal ionicity of the nucleating bonds, enhancing the formation of phase-pure ZB domains.<sup>[46–48]</sup>

Overall, this drastic, nearly tenfold decrease in twin defect density is quite remarkable, considering the very small range of Sb-content over which this observation is made. Strong changes in twin defect density of non-catalytic NWs are, otherwise, often observed when NW diameters vary significantly,<sup>[49,50]</sup> but this effect can be ruled out since the actual diameters vary within less than 5% between the NWs probed from the samples with lowest and highest Sb-flux (i.e.,  $D \approx 174$  nm versus  $D \approx 183$  nm). Hence, our data confirm that the strong changes in microstructure are a direct signature mediated by the Sb action. For comparison, equivalent studies performed on VLS-GaAsSb NWs have shown that much higher Sb-content was necessary to induce such large decrease in twin defect density: For example,  $\approx 20$ -fold higher  $\Phi_{\text{Sb}}/\Phi_{\text{As}}$  ( $\approx 4$ – $32\%$ ; Sb-contents not given),<sup>[25]</sup>  $\approx$  fivefold higher Sb contents ( $\approx 6$ – $27\%$ )<sup>[23,42]</sup> or even pure binary GaSb NWs<sup>[51,52]</sup> were required, where the addition of Sb affects the supersaturation levels and stabilizes the ZB phase in GaAsSb NWs.<sup>[25,27]</sup> Similarly, low twin densities were also observed in VLS-grown InAsSb NWs, but only for Sb content greater than 10%,<sup>[53–56]</sup> and even in VS-grown catalyst-free InAsSb NWs for Sb content of 15–25%.<sup>[29,57,58]</sup>

Further, very interesting observations with respect to the twin defect formation and related influences by the presence of Sb are made from investigations of STEM Z-contrast (atomic number contrast) and compositional maps using energy-dispersive X-ray (EDX) spectroscopy. In Figures 4d and 4e, we show regular STEM-HAADF images and corresponding EDX maps of the Sb-distribution, recorded in the top region of GaAsSb NWs grown with the lowest and highest Sb-BEP, respectively. For low Sb-BEP ( $1 \times 10^{-7}$  mbar), both the STEM image and EDX map exhibit overall homogeneous contrast throughout the NW. On the contrary, for high Sb-BEP ( $9 \times 10^{-7}$  mbar), faint but very distinct contrast modulations are observed in both maps. These modulations run along orientations coinciding with the main low-index growth facets, namely the (111)B growth plane as well as inclined  $\{-1-10\}$  facets (marked as green and purple arrows, respectively). Modulations with dark contrast along these facets correspond to regions of lower Sb incorporation, as seen by the EDX map.

To describe the formation of these peculiar features, we need to comprehend the underlying twin-induced growth mechanism governing the vapor-solid growth of III-V NWs. As noted in detail in ref. [32] (and references therein), growth of vertically oriented NWs proceeds by a competition between the vertical (111)B top facet and a set of threefold symmetric, inclined  $\{-1-10\}$  facets, which intersect with the top facet. During NW growth, the  $\{-1-10\}$  facets are usually slow-growing facets, whereas growth along the (111)B top facet occurs much faster. Hence, the  $\{-1-10\}$  inclined facets grow in size and extend towards the center, as evidenced by the contrast modulations parallel to the inclined  $\{-1-10\}$  planes (purple arrows). Under equilibrium conditions, the convergence of these  $\{-1-10\}$  facets may lead to the formation of a tetrahedral NW tip, and, thus, growth termination.<sup>[32]</sup> However, as pointed out in previous work,<sup>[32,59]</sup> before reaching full convergence, it becomes energetically favorable for a rotational twin to form, which changes

the hierarchy of the growth velocities in the facets of the subsequent layer growth on top. Through this rotation, new tilted  $\{-1-10\}$  facets are generated, which no longer represent slow growing facets, but become fast growing ones, whereas growth along (111)B direction is slowed down. Thereby, a mesa is formed which grows rapidly in the lateral direction and fills up the space above the original  $\{-1-10\}$  facet, resulting in a completely extended (111)B top facet across the entire NW cross-section. The slow growth along the vertical (111)B direction generates, thereby, the observed thin contrast modulation running across the whole diameter of the NW (green arrow, see Figure 4e). After completion of the hexagonal mesa, growth then resumes in the same repetitive manner, that is, starting all over by formation of slow-growing  $\{-1-10\}$  inclined facets, fast growing (111)B top facet, until the next twin forms, etc. Consecutive growth proceeds then by the repetitive pile up of twins, one after another, and results in the periodic contrast modulation pattern observed along the NW growth axis.

The logical question arising now is as to why this characteristic pattern, that demarcates slow growing facets right at the stage of twin formation, is so prominent in the NW grown under highest Sb-supply and why this results in lower Sb-incorporation. Note, the average Sb-content measured by EDX in the thin regions of slow growing facets is as low as 2.8%, while it is about twice as large (5.6%) in the faster growing regions around it (i.e., close to the XRD-measured Sb-content, Figure 2d). This observation can be directly linked to the anticipated Sb surface segregation layer model that describes the incorporation dynamics under large Sb-supply. As argued before, on highly Sb-enriched surfaces (anti-surfactant regime), the incorporation of Sb competes strongly with the detrimental Sb-As exchange reaction.<sup>[33–35]</sup> This exchange reaction is, in fact, highly dependent on growth rate, as observed in literature on planar GaAsSb thin films<sup>[33,35]</sup>—that is, when growth rate is slow, the exchange of Sb and As adatoms has much more time to proceed, consequently lowering Sb incorporation, as opposed to high growth rates. We observe exactly this behavior in our NW, which corroborates the existence of an Sb-rich surface layer limiting the growth and compositional uniformity under excess Sb supply. Adjusting the Sb surface layer to sub-critical coverage, and thereby suppressing the Sb-As exchange reaction, is therefore instrumental in achieving high compositional uniformity, as demonstrated for NWs grown under lower Sb supply.

#### 2.4. Sb-Mediated Optical Properties

To correlate the influence of composition and the altered microstructure on the optical properties, we performed steady-state micro-photoluminescence ( $\mu$ PL) measurements on the respective GaAsSb NWs at low temperature (10 K) and under varying excitation power density ( $P_{\text{exc}}$ ) from  $P_0 = 0.02 \mu\text{W } \mu\text{m}^{-2}$  to  $50P_0$ . The PL spectra obtained from the single NWs grown under the three different Sb fluxes (Sb-content) are illustrated in Figure 5a–c; Sb-BEP of  $1 \times 10^{-7}$  mbar (blue),  $3 \times 10^{-7}$  mbar (green), and  $9 \times 10^{-7}$  mbar (red), respectively. We clearly observe that increasing average Sb-content results in distinct red-shifts of the PL spectra with peak emission centered at  $\approx 1.5$  eV,  $\approx 1.47$  eV,

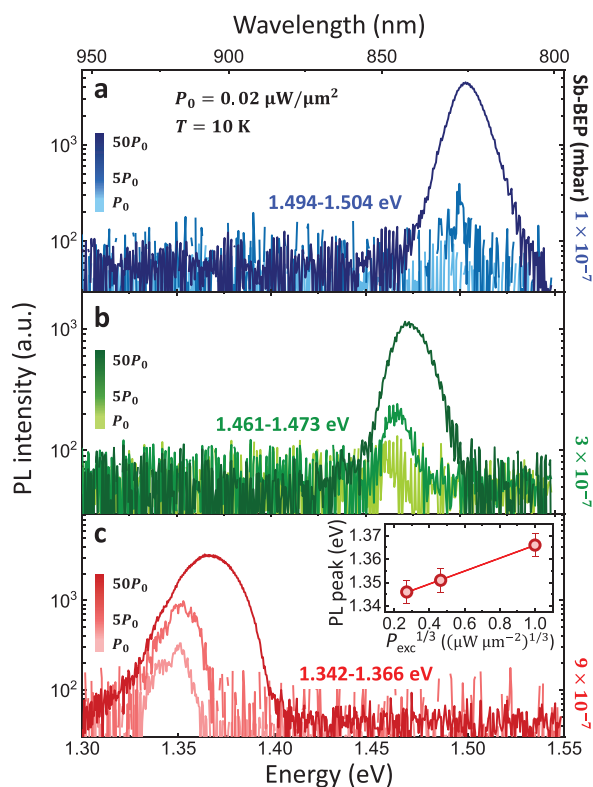


**Figure 5.** Excitation power density ( $P_{\text{exc}}$ )-dependent  $\mu\text{PL}$  spectra on a logarithmic scale obtained from single GaAsSb NWs with varying Sb-BEP of a)  $1 \times 10^{-7}$  mbar, b)  $3 \times 10^{-7}$  mbar, and c)  $9 \times 10^{-7}$  mbar recorded at low-temperature (10 K). The inset plots the PL peak energy shift as a function of  $P_{\text{exc}}^{1/3}$  with a linear fit.

and  $\approx 1.35$  eV, respectively. This red-shift arises, as expected, from the overall reduced bandgap energy upon increasing Sb-content; but also from the different nature of the excitonic transitions mediated by the band offsets between ZB domains and single twin-defect inclusions, which represent ML-thin inclusions of WZ-phase. Such ZB/WZ/ZB crystal interfaces are well known to be characterized by a staggered band lineup for GaAs- and GaSb-materials alike,<sup>[60,61]</sup> which induces a type-II excitonic transition, as verified comprehensively in refs. [62,63]. As illustrated in **Figure 6c**, from a structural point of view, recombination takes, therefore, place essentially between electrons confined in ZB domains with spatially separated holes confined at fixed energy level in adjacent twin defects.<sup>[62,63]</sup> For low and intermediate Sb-content, the twin domain segment length is relatively short,  $\approx 3.3 \pm 0.11$  nm (Sb-BEP =  $1 \times 10^{-7}$  mbar) and  $6.7 \pm 0.44$  nm (Sb-BEP =  $3 \times 10^{-7}$  mbar) (cf. **Figure 4**), and hence electrons localized in the ZB domains are relatively strongly confined. In contrast, for higher Sb-content (Sb-BEP =  $9 \times 10^{-7}$  mbar), the domain lengths are much longer ( $\approx 25 \pm 13$  nm) such that electrons can be considered as unconfined and quasi-free. As a result, the emission energy of quasi-free, delocalized electrons recombining from the band-edge of the ZB domain with holes in twin defects is much red-shifted as opposed to recombination from confined electrons when the domain lengths are very short. Also, the type-II nature of the

transition is expected to be stronger as the electron wavefunction distribution is spatially much more extended for such long ZB domain lengths. This may explain why the PL emission is quite substantially red-shifted in the NWs shown in **Figure 5c** (longest twin-free segment length), much more than what is expected from the pure Sb-mediated band gap effect. Indeed, compared to low-temperature PL data of planar GaAsSb thin films with similar Sb-content,<sup>[64]</sup> the emission of our GaAsSb NWs (6% Sb-content) is red-shifted by  $>50$  meV. At this point, we wish to emphasize that the additional composition modulation (locally lower Sb-content) seen in the twin-defect regions of this NW (cf. **Figure 4e**) will barely affect the quasi-free nature of the electrons, since this modulation only increases the band-offset at the twin boundaries.

Besides the redshifts, the PL data further show several other interesting effects: First, for low to intermediate Sb-content (**Figure 5a,b**) the PL exhibits single-peak emission with symmetric Gaussian shape under low excitation power density, suggesting homogeneous Sb alloy throughout the NWs. The PL peak width evaluated at highest recorded excitation power ( $50P_0$ ) is relatively constant and on the order of  $\approx 17$ – $22$  meV for both these samples. In contrast, the NW with highest Sb-content exhibits multi-peak emission at low  $P_{\text{exc}}$  (**Figure 5c**), with peaks merging upon increasing  $P_{\text{exc}}$ , leading to overall broadened PL peak width of  $\approx 32$  meV at  $50P_0$ . Still even at the highest excitation power, we observe a signature (shoulder) on the low energy side of the spectrum. We suspect that this feature is not defect-related, since, as explained above, this NW has overall lowest twin defect density with very long twin domains, such that recombination occurs from quasi-free, unconfined electrons and holes at fixed energy levels. Instead, we believe that the asymmetrically broadened PL towards the low-energy side stems rather from Sb-related alloy fluctuations that induce localized states.<sup>[65]</sup>

Furthermore, we recognize that all samples exhibit a characteristic blue-shift of the PL peak emission with increasing  $P_{\text{exc}}$ ; yet, the NW with longest domain segment length (Sb-BEP =  $9 \times 10^{-7}$  mbar, **Figure 5c**) shows the most pronounced blue-shift of more than 20 meV over the investigated excitation power range. This is a direct manifestation of the stronger type-II nature of the radiative transition in this NW, due to the much reduced spatial overlap of electron-hole (e-h) pairs for very extended ZB domains. To verify this, we plotted the peak position as a function of the excitation power density (inset of **Figure 5c**), and found that the emission follows closely a cube-root dependence on  $P_{\text{exc}}$ . This  $P_{\text{exc}}^{1/3}$  dependence is very typical for type-II systems, as demonstrated in many reports.<sup>[66,67]</sup> Hence, we can attribute the strong blue-shift in these NWs to the pronounced type-II transition, and not to state-filling as otherwise considered in systems with larger e-h pair overlap.

These characteristics are further revealed by time-resolved photoluminescence (TRPL) experiments, where changes in the spatial overlap of e-h pairs due to different domain segment lengths are expected to yield different excitonic decay times. TRPL decay curves obtained from the same NWs with varying Sb flux are plotted in **Figure 6a**, where the data was recorded at low excitation power density ( $P_{\text{exc}} = 0.1 \mu\text{W} \mu\text{m}^{-2}$ ) at 10 K to inhibit carrier escape and fitted with IRF-convoluted bi-exponential curves. The information about the localized exciton



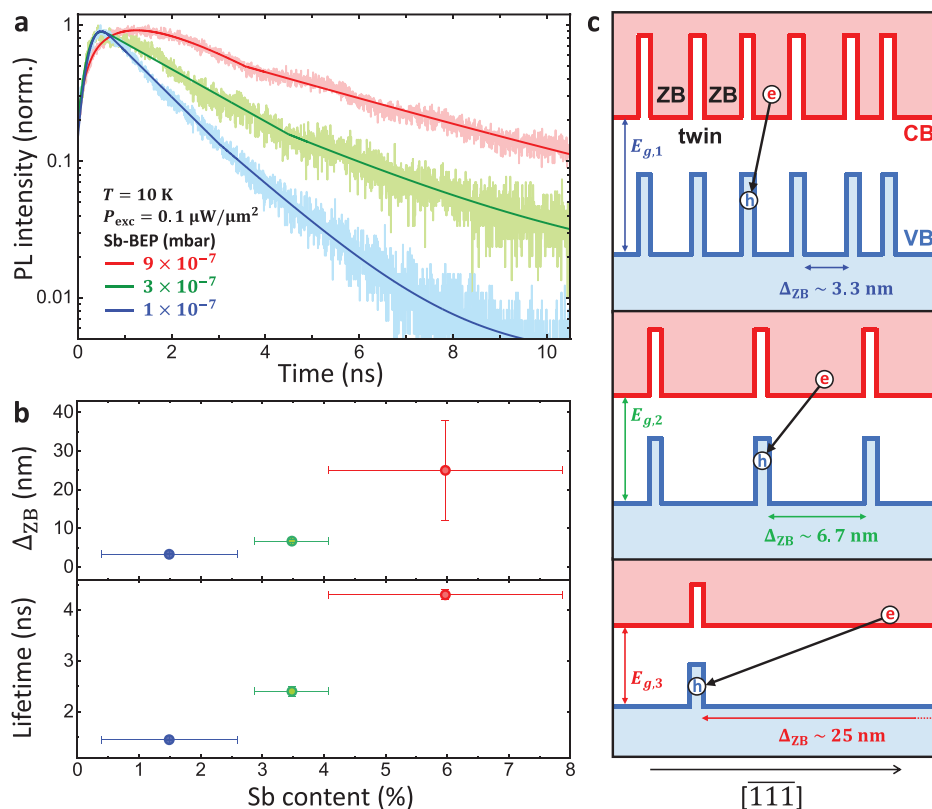


**Figure 6.** a) TRPL decay transients from single GaAsSb NWs at 10 K with varying Sb-BEP, with IRF-convoluted bi-exponential fitting curves. b) Plots of average ZB domain lengths (top) and TRPL-extracted exciton lifetime (bottom) as a function of Sb-content, as measured by HRXRD (Section 2.1). Different colors represent the varying Sb-BEP of  $1 \times 10^{-7}$  (blue),  $3 \times 10^{-7}$  (green), and  $9 \times 10^{-7}$  mbar (red), respectively. c) Schematic illustration of the band profile with different twin densities and domain length  $\Delta_{ZB}$  for each sample, and resulting exciton recombination processes indicated by arrows.  $E_{g,1} > E_{g,2} > E_{g,3}$  represent Sb-content dependent bandgap energies of the GaAsSb NWs.

dynamics, that is, the indirect type-II transitions can thus be extracted from the slow decay component of such stretched exponential tail, while the initial faster decay component represents the dynamics in the quasi-continuum states.<sup>[28,68]</sup> Hence, the slow decay component describes the long-lived transitions due to the spatial separation of e-h pairs in adjacent twin domains, evidencing that the exciton lifetimes increase with increasing Sb-flux, that is, domain segment length. To quantitatively correlate the microstructural data with the localized exciton dynamics, Figure 6b displays the mean twin-free domain length (top) and the extracted exciton lifetime (bottom) as a function of Sb-content in the GaAsSb NWs. We clearly see that with increasing domain length upon increasing Sb-content, the exciton lifetime increases accordingly from  $\approx 1.5$  ns to  $\approx 4.5$  ns. These characteristics can be well understood by the schematics depicted in Figure 6c, where the corresponding band profiles and associated indirect transitions are shown for different domain lengths at varying Sb flux. Under this representation it becomes clear that the spatial overlap of e-h wavefunctions is largest in NWs with small domain length (high twin defect density), while the overlap is strongly reduced for larger domain lengths (small twin defect density). Therefore, the type-II transition appears more pronounced leading to longer lifetimes and stronger excitation power dependent blue-shifts observed in the steady-state PL data. This behavior

is further supported by excitation power dependent TRPL data (Figure S4, Supporting Information), which illustrate shortened lifetimes with increasing power as a result of increasing e-h pair overlap and eventually carrier escape.

### 3. Conclusion

We provided a comprehensive investigation of the growth dynamics and structure-property relationships of novel, catalyst-free GaAsSb NWs grown by selective area MBE under various growth and array geometry parameters. Threshold Sb traces as low as  $\approx 1\%$  lead to strong growth enhancement, which further increases with Sb content up to 3–4%, evidencing a characteristic surfactant effect. The Sb-mediated surfactant action is directly reflected by nearly an order of magnitude increase in the Ga adatom diffusion length (several  $\mu\text{m}$ -long) on the NW sidewalls, as compared to Sb-free GaAs NWs. Growth dynamics then change to anti-surfactant behavior by increasing Sb content to about  $\approx 6\%$ , which is explained by an underlying Sb-As exchange reaction mediated by an Sb-rich surface segregation layer under excess Sb supply. The Sb-As exchange reaction is also found to induce characteristic compositional modulations along the NW growth direction, which coincide with stages of twin defect formation. Remarkably, even over very

narrow compositional range (1.5–6% Sb) the incorporation of Sb leads to nearly tenfold reduction in twin defect density, that is, extended lengths of twin-free ZB segments, exhibiting much stronger influences as commonly found in VLS-type GaAsSb NWs. Larger spatial separation of the e-h pairs in extended twin-free domains significantly enhances the localized exciton lifetime. These results highlight that the addition of Sb in the limit of small compositional ranges is a decisive parameter in tuning the growth- and exciton dynamics in the non-catalytic GaAsSb NWs, paving the pathway for the development of functional nanowire devices.

## 4. Experimental Section

**Selective-Area Molecular Beam Epitaxy:** The growth of GaAsSb NWs was performed in a solid-source Gen-II MBE system equipped with conventional effusion cells for group-III elements (In, Ga, Al) and Veeco valved cracker cells for supplying group-V elements (As, Sb). The As species were supplied as uncracked As<sub>4</sub>, and the Sb species as Sb<sub>2</sub> molecules. For the fabrication of the SAE growth templates, commercial single-side polished 2-inch p-type Si (111) wafers were used as substrates, which are coated with a thermally grown ≈20 nm-thick SiO<sub>2</sub> mask layer on the surface. Using electron beam lithography (EBL) followed by reactive ion etching (RIE) and wet chemical etching (buffered hydrofluoric (HF) acid), the SiO<sub>2</sub> mask layer was prepatterned to induce site-selective NW growth from periodically arranged openings with varying nominal circular opening diameters ( $d_0 = 20\text{--}120$  nm) and pitch ( $p$ ) of 500 nm (unless otherwise noted).<sup>[28,36]</sup> The non-catalytic vertical NW growth was initiated following the same procedures as in the earlier work<sup>[28,29]</sup>; first a substrate annealing step at high-temperature (870 °C) was employed under high As-BEP of  $5.5 \times 10^{-5}$  mbar to stabilize an As-terminated  $1 \times 1$  reconstructed Si (111) surface, which enables high-yield SAE growth. After cooling down to a growth temperature of 630 °C, GaAsSb NWs were grown by simultaneously opening the Ga and Sb shutters. All samples were grown using Ga flux of  $0.35 \text{ \AA s}^{-1}$  and As-BEP of  $5.5 \times 10^{-5}$  mbar, respectively, for a fixed growth time of 90 min (unless otherwise noted). To tune the Sb content in the GaAsSb NWs, the Sb-flux was varied based on the desired fractional flux relative to the As-flux ( $FF_{\text{Sb}} = \Phi_{\text{Sb}_2} / \Phi_{\text{As}_4}$ ). In this study,  $FF_{\text{Sb}}$  of 0.2, 0.5 and 1.6% was applied; that is, corresponding to Sb-BEP of  $1 \times 10^{-7}$ ,  $3 \times 10^{-7}$  and  $9 \times 10^{-7}$  mbar, respectively. For comparison, also an Sb-free GaAs NW reference sample was grown. To further investigate the role of Sb on the time-dependent growth dynamics, another series of GaAsSb NWs with a fixed Sb-BEP of  $3 \times 10^{-7}$  mbar was grown with varying growth times ( $t_{\text{growth}}$ ) from 15 min to 150 min. Likewise, an Sb-free GaAs NW growth time series was grown with  $t_{\text{growth}}$  ranging from 15 min to 120 min, respectively. For optical studies, a coaxial 5-nm thin Al<sub>0.3</sub>Ga<sub>0.7</sub>As surface passivation layer was additionally grown to prevent non-radiative surface recombination, followed by a 3 nm GaAs cap to protect the AlGaAs layer from oxidation.<sup>[69]</sup>

**Morphology and Compositional Analysis:** To analyze the morphology, aspect ratio (length/diameter) and growth yield of the as-grown NW arrays, scanning electron microscopy (SEM) was conducted using an NVision 40 FIB-SEM from Carl Zeiss. All images were recorded at 45° bird-eye view and tilt corrected by the SEM software, displaying real lengths. The alloy composition (Sb-content) of the NW arrays was obtained by 2theta-omega ( $2\theta - \omega$ ) scans in high-resolution X-ray diffraction (HRXRD) using a Rigaku SmartLab diffractometer. To guarantee accurate composition analysis, all samples were aligned and optimized with respect to the Si (111) diffraction peak of the substrate, and the composition calculated using Vegard's law.

**Microstructural Analysis:** High-resolution (HR-) and high-angle annular dark-field scanning transmission electron microscopy (HAADF-STEM) was performed to characterize the microstructural properties of individual GaAsSb NWs, which were mechanically transferred from

identical SAE fields onto carbon-coated copper grids and probed in a FEI Titan Themis TEM operating at 300 kV. For the TEM analysis, the size of the selected area diffraction (SAD) aperture was adjusted to the full length of the NW to obtain representative diffraction pattern information of the entire NW. On selected samples, additional energy-dispersive X-ray (EDX) measurements were performed to characterize compositional profiles, especially elemental Sb distribution throughout the NW.

**Optical Measurements:** Excitation power density ( $P_{\text{exc}}$ ) dependent steady-state and time-resolved confocal  $\mu$ PL measurements were conducted on single NWs dispersed from selected SAE-fields ( $p = 500$  nm and  $d_0 = 70$  nm) onto Si substrates. All samples were placed in a He-flow cryostat (10 K) and excited using a mode-locked tunable Ti:Sapphire laser (780 nm) with a repetition rate of 80 MHz and a pulse width of ≈100 ps. The excitation spot size was ≈1.9  $\mu\text{m}$  focused by an objective lens with NA = 0.42. Since the probed NWs have lengths of ≈1.3  $\mu\text{m}$  or smaller, the entire length of each NW was thereby excited. TRPL measurements were carried out via time correlated single photon counting (TCSPC) using a single-photon Si avalanche diode (SPAD) with a time resolution of <365 ps and a PicoHarp 300 module. All TRPL data was obtained over the entire PL spectral range, that is, the emission was not spectrally resolved, and fitting of exponential decay was convoluted with the instrument response function (IRF) of the experimental system.

## Supporting Information

Supporting Information is available from the Wiley Online Library or from the author.

## Acknowledgements

The authors gratefully acknowledge support from the European Research Council (ERC project QUANTIC, ID: 771747), and the Deutsche Forschungsgemeinschaft (DFG) via Germany's Excellence Strategy-EXC-2111-390814868 (Munich Center for Quantum Science and Technology, MCQST). The authors also thank Paul Schmiedeke for helpful discussions, Hubert Riedl for technical support with MBE, and Michael Böhmer for providing the electronic signal converter of TRPL setup.

Open access funding enabled and organized by Projekt DEAL.

## Conflict of Interest

The authors declare no conflict of interest.

## Author Contributions

H.W.J. and A.A. contributed equally to this work. H.W.J. wrote the manuscript in consultation with G.K., and all authors contributed to the final manuscript. A.A., H.W.J., and G.K. conceived this work and planned the experiments. N.M. and H.W.J. carried out SAE template design and fabrication with contributions from A.A., and A.A. performed MBE growths. H.Y., H.W.J., and A.A. conducted SEM measurements and analysis. A.A. and H.Y. carried out XRD measurements and analysis. M.D. performed STEM and EDX measurements on the samples prepared by H.W.J., and M.D. and H.W.J. analyzed the resulting data. H.W.J. implemented optical measurements and data analysis. G.K. and J.J.F. supervised the project.

## Data Availability Statement

The data that support the findings of this study are available from the corresponding author upon reasonable request.

## Keywords

exciton dynamics, GaAsSb nanowires, photoluminescence, rotational twin defects, selective-area molecular beam epitaxy

Received: December 2, 2022

Revised: January 3, 2023

Published online: January 20, 2023

- [1] T. Bryllert, L.-E. Wernersson, L. E. Froberg, L. Samuelson, *IEEE Electron Device Lett.* **2006**, *27*, 323.
- [2] K. Tomioka, M. Yoshimura, T. Fukui, *Nature* **2012**, *488*, 189.
- [3] J. A. Czaban, D. A. Thompson, R. R. LaPierre, *Nano Lett.* **2009**, *9*, 148.
- [4] J. Wallentin, N. Anttu, D. Asoli, M. Huffman, I. Åberg, M. H. Magnusson, G. Siefer, P. Fuss-Kailuweit, F. Dimroth, B. Witzigmann, H. Q. Xu, L. Samuelson, K. Deppert, M. T. Borgström, *Science* **2013**, *339*, 1057.
- [5] P. Krogstrup, H. I. Jørgensen, M. Heiss, O. Demichel, J. V. Holm, M. Aagesen, J. Nygard, A. Fontcuberta i Morral, *Nat. Photonics* **2013**, *7*, 306.
- [6] I. Åberg, G. Vescovi, D. Asoli, U. Naseem, J. P. Gilboy, C. Sundvall, A. Dahlgren, K. E. Svensson, N. Anttu, M. T. Björk, L. Samuelson, *IEEE J. Photovoltaics* **2016**, *6*, 185.
- [7] D. Saxena, S. Mokkapatil, P. Parkinson, N. Jiang, Q. Gao, H. H. Tan, C. Jagadish, *Nat. Photonics* **2013**, *7*, 963.
- [8] J. Tatebayashi, S. Kako, J. Ho, Y. Ota, S. Iwamoto, Y. Arakawa, *Nat. Photonics* **2015**, *9*, 501.
- [9] B. Mayer, L. Janker, B. Loitsch, J. Treu, T. Kostenbader, S. Lichtmannecker, T. Reichert, S. Morkötter, M. Kaniber, G. Abstreiter, C. Gies, G. Koblmüller, J. J. Finley, *Nano Lett.* **2016**, *16*, 152.
- [10] H. Kim, D. Ovchinnikov, D. Deiana, D. Unuchek, A. Kis, *Nano Lett.* **2017**, *17*, 5056.
- [11] K. Tomioka, J. Motohisa, S. Hara, K. Hiruma, T. Fukui, *Nano Lett.* **2010**, *10*, 1639.
- [12] E. Dimakis, U. Jahn, M. Ramsteiner, A. Tahraoui, J. Grandal, X. Kong, O. Marquardt, A. Trampert, H. Riechert, L. Geelhaar, *Nano Lett.* **2014**, *14*, 2604.
- [13] B. Loitsch, J. Winnerl, G. Grimaldi, J. Wierzbowski, D. Rudolph, S. Morkötter, M. Döblinger, G. Abstreiter, G. Koblmüller, J. J. Finley, *Nano Lett.* **2015**, *15*, 7544.
- [14] L. Leandro, C. P. Gunnarsson, R. Reznik, K. D. Jöns, I. Shtrom, A. Khrebtov, T. Kasama, V. Zwiller, G. Cirlin, N. Akopian, *Nano Lett.* **2018**, *18*, 7217.
- [15] N. Mukhundan, A. Ajay, J. Bissinger, J. J. Finley, G. Koblmüller, *Opt. Express* **2021**, *29*, 43068.
- [16] L. Ma, X. Zhang, H. Li, H. Tan, Y. Yang, Y. Xu, W. Hu, X. Zhu, X. Zhuang, A. Pan, *Semicond. Sci. Technol.* **2015**, *30*, 105033.
- [17] Z. Li, X. Yuan, L. Fu, K. Peng, F. Wang, X. Fu, P. Caroff, T. P. White, H. H. Tan, C. Jagadish, *Nanotechnology* **2015**, *26*, 445202.
- [18] J. Sun, M. Peng, Y. Zhang, L. Zhang, R. Peng, C. Miao, D. Liu, M. Han, R. Feng, Y. Ma, Y. Dai, L. He, C. Shan, A. Pan, W. Hu, Z. Yang, *Nano Lett.* **2019**, *19*, 5920.
- [19] L. Cerutti, J. B. Rodriguez, E. Tournie, *IEEE Photon. Technol. Lett.* **2010**, *22*, 553.
- [20] J.-B. Wang, S. R. Johnson, S. A. Chaparro, D. Ding, Y. Cao, Y. G. Sadofyev, Y.-H. Zhang, J. A. Gupta, C. Z. Guo, *Phys. Rev. B* **2004**, *70*, 195339.
- [21] J. Huh, H. Yun, D.-C. Kim, A. M. Munshi, D. L. Dheeraj, H. Kauko, A. T. J. van Helvoort, S. Lee, B.-O. Fimland, H. Weman, *Nano Lett.* **2015**, *15*, 3709.
- [22] D. Ren, L. Ahtapodov, J. S. Nilsen, J. Yang, A. Gustafsson, J. Huh, G. J. Conibeer, A. T. J. van Helvoort, B.-O. Fimland, H. Weman, *Nano Lett.* **2018**, *18*, 2304.
- [23] S. Conesa-Boj, D. Kriegner, X.-L. Han, S. Plissard, X. Wallart, J. Stangl, A. Fontcuberta i Morral, P. Caroff, *Nano Lett.* **2014**, *14*, 326.
- [24] X. Yuan, P. Caroff, J. Wong-Leung, H. H. Tan, C. Jagadish, *Nanoscale* **2015**, *7*, 4995.
- [25] D. Ren, D. L. Dheeraj, C. Jin, J. S. Nilsen, J. Huh, J. F. Reinertsen, A. M. Munshi, A. Gustafsson, A. T. J. van Helvoort, H. Weman, B.-O. Fimland, *Nano Lett.* **2016**, *16*, 1201.
- [26] L. Li, D. Pan, Y. Xue, X. Wang, M. Lin, D. Su, Q. Zhang, X. Yu, H. So, D. Wei, B. Sun, P. Tan, A. Pan, J. Zhao, *Nano Lett.* **2017**, *17*, 622.
- [27] D. L. Dheeraj, G. Patriarche, L. Largeau, H. L. Zhou, A. T. J. van Helvoort, F. Glas, J. C. Harmand, B. O. Fimland, H. Weman, *Nanotechnology* **2008**, *19*, 275605.
- [28] A. Ajay, H. Jeong, T. Schreitmüller, M. Döblinger, D. Ruhstorfer, N. Mukhundan, P. Koolen, J. J. Finley, G. Koblmüller, *Appl. Phys. Lett.* **2022**, *121*, 072107.
- [29] D. Ruhstorfer, S. Mejia, M. Ramsteiner, M. Döblinger, H. Riedl, J. J. Finley, G. Koblmüller, *Appl. Phys. Lett.* **2020**, *116*, 052101.
- [30] G. Koblmüller, S. Hertenberger, K. Vizbaras, M. Bichler, F. Bao, J. P. Zhang, G. Abstreiter, *Nanotechnology* **2010**, *21*, 365602.
- [31] K. Ikejiri, T. Sato, H. Yoshida, K. Hiruma, J. Motohisa, S. Hara, T. Fukui, *Nanotechnology* **2008**, *19*, 265604.
- [32] D. Ruhstorfer, M. Döblinger, H. Riedl, J. J. Finley, G. Koblmüller, *J. Appl. Phys.* **2022**, *132*, 204302.
- [33] R. Kaspi, K. R. Evans, *J. Cryst. Growth* **1997**, *175/176*, 838.
- [34] Z. Zhang, K. Ghosh, N. N. Faleev, H. Wang, C. B. Honsberg, P. Reece, S. P. Bremner, *J. Cryst. Growth* **2019**, *526*, 152321.
- [35] T. Zederbauer, A. M. Andrews, D. MacFarland, H. Detz, W. Schrenk, G. Strasser, *APL Mater.* **2017**, *5*, 035501.
- [36] D. Ruhstorfer, A. Lang, S. Matich, M. Döblinger, H. Riedl, J. J. Finley, G. Koblmüller, *Nanotechnology* **2021**, *32*, 135604.
- [37] Z. Kollonitsch, K. Möller, F. Willig, T. Hannappel, *J. Cryst. Growth* **2004**, *272*, 694.
- [38] J.-C. Harmand, L. H. Li, G. Patriarche, L. Travers, *Appl. Phys. Lett.* **2004**, *84*, 3981.
- [39] M. T. Björk, H. Schmid, C. M. Breslin, L. Gignac, H. Riel, *J. Cryst. Growth* **2012**, *344*, 31.
- [40] F. Del Giudice, J. Becker, C. de Rose, M. Döblinger, D. Ruhstorfer, L. Suomenniemi, J. Treu, H. Riedl, J. J. Finley, G. Koblmüller, *Nanoscale* **2020**, *12*, 21857.
- [41] V. G. Dubrovskii, *ACS Omega* **2019**, *4*, 8400.
- [42] D. L. Dheeraj, G. Patriarche, H. Zhou, T. B. Hoang, A. F. Moses, S. Grønsberg, A. T. J. van Helvoort, B.-O. Fimland, H. Weman, *Nano Lett.* **2008**, *8*, 4459.
- [43] D. Spirkoska, J. Arbiol, A. Gustafsson, S. Conesa-Boj, F. Glas, I. Zardo, M. Heigoldt, M. H. Gass, A. L. Bleloch, S. Estrade, M. Kaniber, J. Rossler, F. Peiro, J. R. Morante, G. Abstreiter, L. Samuelson, A. Fontcuberta i Morral, *Phys. Rev. B* **2009**, *80*, 245325.
- [44] D. Rudolph, S. Hertenberger, S. Bolte, W. Paosangthong, D. Spirkoska, M. Doeblinger, M. Bichler, J. J. Finley, G. Abstreiter, G. Koblmüller, *Nano Lett.* **2011**, *11*, 3848.
- [45] D. T. J. Hurler, P. Rudolph, *J. Cryst. Growth* **2004**, *264*, 550.
- [46] N. E. Christensen, S. Satpathy, Z. Pawlowska, *Phys. Rev. B* **1987**, *36*, 1032.
- [47] H. Abu-Farsakh, A. Qteish, *Phys. Rev. B* **2007**, *75*, 085201.
- [48] H. Weman, D. L. Dasa, *Adv. III-V Semicond. Nanowires Nanodevices* **2011**, 89.
- [49] H. Yoshida, K. Ikejiri, T. Sato, S. Hara, K. Hiruma, J. Motohisa, T. Fukui, *J. Cryst. Growth* **2009**, *312*, 52.
- [50] J. N. Shapiro, A. Lin, C. Ratsch, D. L. Huffaker, *Nanotechnology* **2013**, *24*, 475601.
- [51] Y. N. Guo, J. Zou, M. Paladugu, H. Wang, Q. Gao, H. H. Tan, C. Jagadish, *Appl. Phys. Lett.* **2006**, *89*, 231917.

- [52] M. Jeppsson, K. A. Dick, J. B. Wagner, P. Caroff, K. Deppert, L. Samuelson, L.-E. Wernersson, *J. Cryst. Growth* **2008**, *310*, 4115.
- [53] B. M. Borg, K. A. Dick, J. Eymery, L.-E. Wernersson, *Appl. Phys. Lett.* **2011**, *98*, 113104.
- [54] W.-N. Du, X.-G. Yang, X.-Y. Wang, H.-Y. Pan, H.-M. Ji, S. Luo, T. Yang, Z.-G. Wang, *J. Cryst. Growth* **2014**, *396*, 33.
- [55] X. Ji, X. Yang, W. Du, H. Pan, T. Yang, *Nano Lett.* **2016**, *16*, 7580.
- [56] Q. D. Zhuang, E. A. Anyebe, R. Chen, H. Liu, A. M. Sanchez, M. K. Rajpalke, T. D. Veal, Z. M. Wang, Y. Z. Yuang, H. D. Sun, *Nano Lett.* **2015**, *15*, 1109.
- [57] M. J. L. Sourribes, I. Isakov, M. Panfilova, H. Liu, P. A. Warburton, *Nano Lett.* **2014**, *14*, 1643.
- [58] H. Potts, M. Friedl, F. Amaduzzi, K. Tang, G. Tütüncüoğlu, F. Matteini, E. A. Lladó, P. C. McIntyre, A. Fontcuberta i Morral, *Nano Lett.* **2016**, *16*, 637.
- [59] M. Yao, C. Sheng, M. Ge, C.-Y. Chi, S. Cong, A. Nakano, P. D. Dapkus, C. Zhou, *ACS Nano* **2016**, *10*, 2424.
- [60] A. Belabbes, C. Panse, J. Furthmüller, F. Bechstedt, *Phys. Rev. B* **2012**, *86*, 075208.
- [61] A. De, C. E. Pryor, *Phys. Rev. B* **2010**, *81*, 155210.
- [62] A. Senichev, P. Corfdir, O. Brandt, M. Ramsteiner, S. Breuer, J. Schilling, L. Geelhaar and, P. Werner, *Nano Res.* **2018**, *11*, 4708.
- [63] M. M. Sonner, M. Gnedel, J. C. Berlin, D. Rudolph, G. Koblmüller, H. J. Krenner, *Nanotechnology* **2021**, *32*, 505209.
- [64] Y. F. Biryulin, R. R. Ichkitidze, V. G. Krigel, V. V. Chaldyshev, Y. V. Shmartsev, *Sov. Phys. Semicond.* **1979**, *13*, 1334.
- [65] X. Gao, Z. Wei, F. Zhao, Y. Yang, R. Chen, X. Fang, J. Tang, D. Fang, D. Wang, R. Li, X. Ge, X. Ma, X. Wang, *Sci. Rep.* **2016**, *6*, 29112.
- [66] Y. S. Chiu, M. H. Ya, W. S. Su, Y. F. Chen, *J. Appl. Phys.* **2002**, *92*, 5810.
- [67] C. Y. Jin, H. Y. Liu, S. Y. Zhang, Q. Jiang, S. L. Liew, M. Hopkinson, *Appl. Phys. Lett.* **2007**, *91*, 021102.
- [68] D. Rudolph, L. Schweickert, S. Morkötter, L. Hanschke, S. Hertenberger, M. Bichler, G. Koblmüller, G. Abstreiter, J. J. Finley, *New J Phys* **2013**, *15*, 113032.
- [69] D. Rudolph, S. Funk, M. Doeblinger, S. Morkoetter, S. Hertenberger, L. Schweickert, J. Becker, S. Matich, M. Bichler, D. Spirkoska, I. Zardo, J. J. Finley, G. Abstreiter, G. Koblmüller, *Nano Lett.* **2013**, *13*, 1522.